UNIVERSITY OF BIRMINGHAM

The influence of processing environment on laser-induced periodic surface structures generated with green nanosecond laser

Karkantonis, Themistoklis; Gaddam, Anvesh; Tao, Xiao; See, Tian; Dimov, Stefan

[Link to publication on Research at Birmingham portal](#)

The influence of processing environment on laser-induced periodic surface structures generated with green nanosecond laser

Themistoklis Karkantonis[1a, *], Anvesh Gaddam[1a], Xiao Tao[1b], Tian Long See[2], Stefan Dimov[1a]

[1a] Department of Mechanical Engineering, School of Engineering, The University of Birmingham, Birmingham, B15 2TT, UK

[1b] School of Metallurgy and Materials research, The University of Birmingham, Birmingham, B15 2TT, UK

[2] The Manufacturing Technology Centre Ltd, Coventry, CV7 9JU, UK

* Corresponding author

E-mail address: TXK880@bham.ac.uk (T. Karkantonis).

Abstract

Laser-induced periodic surface structures (LIPSS) are nanometric surface undulations produced by short and ultrashort pulsed lasers. The production of high-quality LIPSS is essential to obtain the required surface responses in various applications. In this work, the LIPSS were fabricated on stainless steel surfaces by a 515 nm nanosecond laser operating under ambient and argon enriched atmospheres to investigate their quality. The LIPSS quality is correlated to the diffracted light intensity and their key geometric parameters such as periodicity and amplitude. The LIPSS formation was observed at an accumulated fluence of above 13.9 J/cm^2 and the optimal processing window was sustained up to 46.2 J/cm^2 before the oxidation occurred. The LIPSS generated in the argon environment exhibited a relatively higher intensity of the diffracted light than those processed in the ambient conditions. Furthermore, LIPSS generated in argon showed minimum surface defects and higher amplitude ripples compared to those in air. The X-ray photoelectron spectroscopy analysis revealed that the ratio of oxygen to metal species decreased in the argon atmosphere and thus minimal surface oxidation occurred on the samples. Since the generation of high-quality LIPSS is a prerequisite for an accurate predictive modeling of surface responses, the results reported here show that good nanostructured surfaces can be produced with cost-effective nanosecond green lasers.

Keywords: Argon, fluence, LIPSS, nanosecond, oxidation, XPS.

1. Introduction

Surface functionalization technologies have received significant attention from industry and research as an important enabler for imparting attractive surface functionalities to products without changing their bulk material properties. In particular, various surface treatment methods, such as coatings, photolithography, chemical etching, sol-gel, ultra-precision machining and laser micro-machining, have been deployed to tailor the functional properties of surfaces by modifying their topography and/or surface microstructure and composition [1-2]. Compared to the other technologies, laser surface texturing (LST) can be considered as a more environmentally friendly process that offers selectivity, relatively high processing accuracy, productivity and even the flexibility of processing freeform surfaces [3]. At the same time, it can be employed as a simple one-step surface treatment to selectively fabricate micron and submicron structures on almost any engineering material without requiring any hazardous chemicals. In addition, LST alters simultaneously the surface chemistry together with the topography, thus, eliminating the need for fluorinated coatings [4].

Laser-induced periodic surface structures (LIPSS) are periodical ripple-like nanostructures that can be imprinted on a variety of materials by employing linearly or azimuthally polarized laser sources [5]. These surface structures can be clustered into low spatial frequency LIPSS (LSFL) and high spatial frequency LIPSS (HSFL) with periodicities close to and much smaller than the laser wavelength, respectively. Among them, only LSFL, referred to as LIPSS in this research, can be obtained both with ultra-short (femtosecond and picosecond) [6] and short (nanosecond) [7] pulse durations and have attracted attention from researchers. Owing to their wide applicability and varying geometrical characteristics, these ripple-like structures have been extensively investigated as a means for functional surface treatments. More specifically, surfaces textured with such nanoscale ripples have displayed anti-bacterial [8-9], anti-icing [10], anti-reflective [11], hydrodynamic drag reduction [12], lubricant-retention [13], secondary electron yield reduction [14] and improved cell-adhesion [15-16] properties in applications related to food packaging, biomedical and energy storage sectors.

Predictive analytical and computational modeling offers the possibility to tailor the surface responses by varying the periodic nanometric geometries in the aforesaid functional applications. For instance, recent efforts employing the computational modeling have shed light on the interaction mechanisms of periodic nanometric surface

2

structures with matter to obtain optimal surface responses in applications related to anti-biofouling [17], hydrodynamic drag reduction [18], anti-reflection [19] and condensation [20]. However, it is imperative to imprint LIPSS homogeneously with sufficient repeatability and reproducibility, and only then the predictive results can be sufficiently accurate within some pre-define limits. To date, most studies have been focused on the use of ultra-short pulse lasers to attain homogeneous LIPSS onto plain and freeform surfaces while maintaining their geometric characteristics within pre-defined ranges [21-22]. Although high precision, controllability and minimum heat-affected zone (HAZ) can be achieved by employing ultrashort lasers, their average power is relatively low and consequently this entails longer processing times. While the usage of multi-beam processing [23] and high repetition rate (MHz or GHz) [24] can reduce the processing time, they increase substantially the required capital investment. As a result of these inherent shortcomings, the broader use of LIPSS treatments in industrial applications is hampered. On the contrary, nanosecond lasers are a cost-effective alternative to treat large surface areas without requiring substantial investments.

One of the main concerns when employing lasers with longer pulse durations for texturing/structuring metallic surfaces is that this is thermal processing with the associated heat-induced negative side effects, i.e., oxidation and re-cast formations on the surface. Nevertheless, it has been shown that the level of laser-induced oxidation can be minimized upon irradiation in a controlled environment when nanosecond lasers are used for polishing operations [25-26]. In general, the use of nanosecond lasers on metals has been mostly limited to the creation of superhydrophobic surfaces by taking advantage of their negative side effects, i.e., by roughening the surface [27] or the fabrication of LIPSS when operating at near-infrared wavelengths [28]. Although the importance of this technology for functionalizing surfaces at an industrial level is recognized through these studies, only a few publications were focused on investigating the generation of LIPSS on metallic substrates using visible wavelengths (400-700 nm) [29-30]. However, some investigations are reported on processing semiconductors [31], polymers [32] and glasses [33-34] using green (500-550 nm) nanosecond pulsed lasers. By operating in the green wavelength regime, nanostructures with a periodicity close to 500 nm can be formed on surfaces.

Nürnberger et al. [29] elucidated the effect of material crystal orientation on the formation of LIPSS when a 532 nm wavelength nanosecond laser was used to process stainless steel and silicon. Simões et al. [30] applied a green nanosecond pulsed laser to investigate the evolution of LIPSS on stainless steel surfaces by employing different process parameters and proposed an approach based on the diffracted light to assess the quality of the LIPSS. However, investigations onto the improvements of the quality and homogeneity of LIPSS have not been reported. In addition, the surface chemical changes of metallic surfaces processed with green nanosecond lasers have not studied earlier. Therefore, this research reports an investigation into the formation, evolution, and properties of LIPSS generated with a green nanosecond pulsed laser on stainless steel substrates under ambient and argon enriched conditions to assess their impact on LIPSS quality. In particular, this research elucidates the influence of processing environment on LIPSS geometrical characteristics, i.e., amplitude and periodicity, and surface chemistry, and subsequently their combined influence on wetting properties. Moreover, the effects of the nanoscale surface topography are analyzed with light diffraction to qualitatively assess their homogeneity.

2. Materials and methods

2.1 Experimental setup and process parameters

The AISI 316 stainless steel (SS) rectangular plates with a 0.5 mm thickness and an average roughness (S_a) of 35 nm were used in the LST experiments. In this work, the as-received substrates were laser textured immediately after removing the plastic tape from surfaces without any pretreatment. The experiments were conducted on the state-of-the-art LASEA LS4 laser micro-machining workstation and its main beam delivery component technologies are shown in Fig. 1a. The platform integrates a s-polarized nanosecond fiber laser source (GLPN -500-1.5-50-M, IPG) with the following main technical characteristics: a pulse duration of 1.5 ns at a nominal wavelength, λ, of 515 nm and pulse repetition rate up to 1 MHz with a maximum average power of 50 W. A scan head (LS-Scan XY 20) is used to steer the laser beam across the samples at a maximum scanning speed of 2 m/s. A telecentric lens with 100 mm focal distance was utilized to focus the laser beam down to a spot size ($2w_0$) of 40 μm at the focal plane. Thereafter, the accurate positioning of the samples inside the machine's working envelope and specifically at the focal plane was performed using a stack of two rotary

and three linear motorized stages in combination with a high-resolution positioning camera (Dino-Lite Premier, AM7013MT).
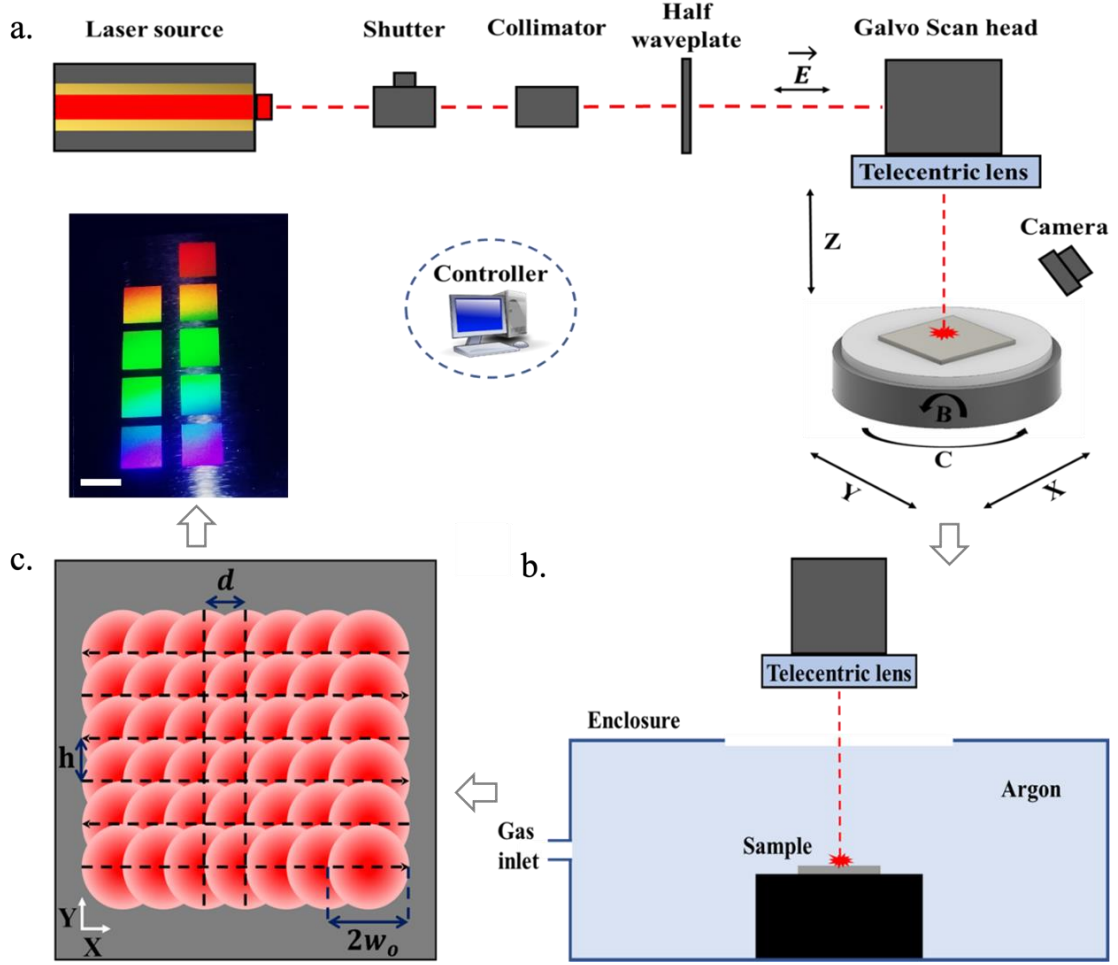

Fig. 1. Schematic illustration of: (a) laser processing set-up. (b) the process used to texture the samples in argon environment. (c) the scanning strategy used to generate LIPSS. The optical image shows diffraction colors resulted from generated LIPSS (scale bar: 10 mm).

To study the generation and evolution of LIPSS on surfaces, the influence of three critical laser processing parameters was investigated, i.e. (i) average power (ii) scanning speed and (iii) hatch distance. The SS substrates were textured by using a horizontal raster scanning strategy as illustrated in Fig. 1c. The distance between successive scanning lines is defined as a hatch one (h), which was varied in the range from 1 to 3 µm. The laser texturing was carried out at various scanning speeds (v) from 0.3 to 2 m/s and average power (P) between 0.189 and 0.671 W. All the experimental trials were conducted at a fixed pulse repetition rate (f) of 100 kHz. As the laser beam was scanned across the surface area, the pulse-to-pulse distance ($d = v/f$) varies and

consequently the effective number of pulses (N_{eff}) or number of pulses per unit area on the surface can be determined from Eq. 1.

$$N_{eff} = \frac{\pi w_0^2}{dh} \qquad (1)$$

Similarly, the substrates were subjected to different pulse fluence (F_0) by varying the average power, and this is calculated with Eq. 2.

$$F_0 = \frac{P}{\pi w_0^2 f} \qquad (2)$$

The combined influence of these two parameters increases the accumulated fluence per unit area (F_{acc}) on the surface, which can be calculated using Eq. 3.

$$F_{acc} = N_{eff}F_0 = \frac{P}{fdh} \qquad (3)$$

Initially, the laser processing was restricted over an area of 5×5 mm^2 on the SS substrates in order to assess the formation of LIPSS on the surface. Thereafter, larger areas of 25×25 mm^2 were textured for investigating their functional response. The experiments were conducted under atmospheric and argon gas environments to investigate their impact on both surface morphology and chemical state after undergoing LIPSS treatments. The laser texturing of samples in a controlled argon gas environment were conducted inside a hollow cylindrical aluminium chamber as illustrated in Fig. 1b. As argon is heavier compared to air, the SS samples were placed at the bottom of the chamber while the gas filled the enclosed area at a constant flow rate of 12 L/min.

2.2 Surface characterization techniques

The surface topographies of the textured SS substrates were initially characterized using a Scanning Electron Microscope (SEM, Hitachi TEM3030Plus). To capture the first-order diffracted light ($m = 1$) out of the treated surfaces, an optical microscope (Alicona G5) was employed by holding a collimated white light beam (70 Lumens) at an incident angle (θ) of 60° relative to the sample surface. Both, the light source and its incident angle were kept constant in regard to the treated surface during the measurements and an open-source image analysis software (ImageJ) was used to obtain the mean intensity (I) of diffracted light. The morphology of the nanoscale topographies was captured by using Atomic Force Microscopy (AFM, MFP-3D, Asylum Research, USA) together with 2D Fast Fourier Transformation (FFT) analysis to evaluate their spatial periods.

The acquired AFM and SEM scan images were analyzed using an open-source image analysis software (Gwyddion).

To inspect the surface chemistry of the substrates produced under air and argon gas environments, the X-ray Photon Spectroscopy (XPS) was conducted by using a Kratos Axis SUPRA spectrometer. These experiments were performed using a monochromatic Al kα (1486.69 eV) X-ray source over an analysis area of 700×300 μm^2, operating at 15 mA emission and 15 kV HT (225W). The instrument was calibrated to gold metal Au 4f (83.95 eV) and dispersion adjusted give a binding energy of 932.6 eV for the Cu2p (3/2) line of metallic copper. The instrumental resolution was determined to be 0.29 eV at 10 eV pass energy using the Fermi edge of the valence band for metallic silver. The survey scans in the range of 0 to 1200 eV binding energy were recorded at pass energies of 160 eV, whilst the high-resolution ones were obtained at pass energies of 40 eV. The step sizes were 1 and 0.1 eV, respectively. Charge neutralization was not required due to high sample conductivity. All data was recorded at a base pressure of below 9×10^{-9} Torr and a room temperature of 294 K. The curve fitting was implemented in CasaXPS v2.3.19PR1.0 using a Shirley background prior to component analysis. O1s components were fit using a lineshape of GL(30).

The wetting properties of the treated surfaces were assessed with a goniometer (OCA 15EC, Data Physics GmbH, Germany). Specifically, water droplets of 4 μL were deposited on the surface and the corresponding static contact angle values were recorded. It is worth noting that the same measurement procedure was repeated five times at different locations on the samples' surfaces to assess the repeatability of the measurements.

3. Results and discussion

3.1 LIPSS evolution and quality in ambient environment

The first part of this research was focused on investigating the LIPSS evolution with a single-pass laser processing in ambient environment. The primary goal was to identify the minimum accumulated fluence required for LIPSS generation on the irradiated surface when operating at high processing speeds, which is a key aspect for their broader implementation in industrial applications. Therefore, the SS substrates were textured with a scanning speed of 2 m/s and different accumulated fluences by adjusting only the average power. As can be seen in Fig. 2, the surface remained intact up to an

accumulated fluence of 12.9 J/cm^2, whilst further increase led to the appearance of LIPSS on the surface. So, the accumulated fluence threshold for the LIPSS generation with an effective number of pulses of 63 was determined to be as low as 13.9 J/cm^2. Thereafter, the irradiation of SS samples was conducted above the predetermined LIPSS threshold with varied pulse fluence but at a fixed effective number of pulses to assess their evolution onto the surface.
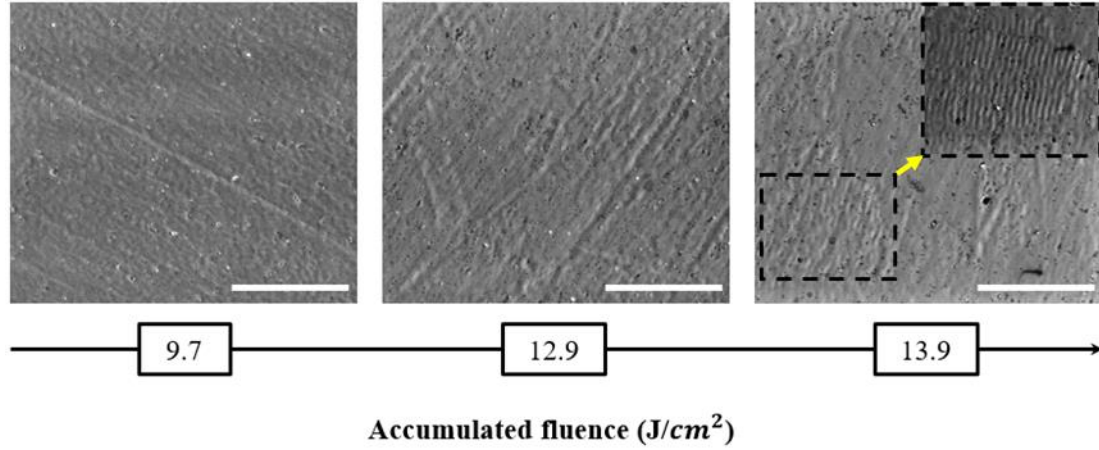

Fig. 2. Evolution of LIPSS with the increase of accumulated fluence at a scanning speed of 2 m/s (scale bar: 10 μm). *Note:* The black dashed rectangle on the upper right corner is a magnified view showing the first LIPSS formation.

The first-order diffracted light was captured from these surfaces to determine the LIPSS quality as illustrated in Fig. 3a. First, the LIPSS spatial periodicity was measured at various pulse fluence levels while keeping the effective number of pulses at 209. To obtain information about their spatial periods, the acquired SEM images of the samples were processed and analyzed by using 2D FFT. The plot in Fig. 3b shows the main spatial periodicities of LIPSS against pulse fluence. As can be seen, the spatial periodicities of LIPSS were below the laser wavelength ($\lambda = 515$ nm) for a normal beam incident angle and varied from 473 to 498 nm. Moreover, the 2D FFT image as shown in Fig. 3c also shows excellent LIPSS regularity at a pulse fluence of 171.2 mJ/cm^2.

Three representative SEM images of LIPSS formation on the surface by increasing pulse fluence are shown in Fig. 3d. Here, the effective number of pulses is 126. For normal beam incidence angle, the orientation of LIPSS was found to be perpendicular to the laser beam polarization vector (indicated by yellow double-sided arrows) regardless of the applied pulse fluence. In the early stage of LIPSS generation, i.e., at $F_o = 153.6$ mJ/cm^2, some pits/holes were observed on the surface which gradually

8

disappeared as the pulse fluence was further increased to 206.2 mJ/cm^2. Typically, the LIPSS begin to develop on the surface between the melting and the ablation threshold of the material [35]. Thus, the formation of these surface defects may be attributed to some low-level heating and consequently not well pronounced melting of the material. These experimental observations confirm the hypothesis that the LIPSS generation upon irradiation with nanosecond pulsed lasers is strongly related to the melting of an adequate layer thickness on the surface [30]. By increasing the pulse fluence further to 220.5 mJ/cm^2, more consistent and pronounced LIPSS formed on the surface. A further increase of pulse fluence beyond 220.5 mJ/cm^2 led again to a gradual LIPSS deterioration, whilst the oxidation effects started to become pronounced at a pulse fluence higher than 261.9 mJ/cm^2.

Since the LIPSS periodicity is 470-500 nm, the first-order diffracted light has wavelength in the same range, which is predominantly blue light. As can be seen in Fig. 3d, the intensity of the blue light emitted from the textured surfaces increased with the increase of LIPSS quality. In addition, the surfaces covered with pits/holes at low pulse fluence did not emit intense blue light when compared to ones without any such defects. Next, the influence of the effective number of pulses on the evolution of LIPSS at a fixed pulse fluence was analyzed. Representative SEM micrographs in Fig 3e depict the LIPSS generated with pulse fluences of 171.2 mJ/cm^2 but with the different effective number of pulses. It is evident that both laser processing parameters had a significant impact on the LIPSS evolution onto the surface. As the distance between two successive pulses decreased and consequently the effective number of pulses increased, the necessary pulse fluence to produce good-quality LIPSS was significantly decreased, too. This is also apparent from the blue light intensity of the corresponding LIPSS topographies. In general, there was a narrow window of pulse fluence up to 220.5 mJ/cm^2 at 209 effective number of pulses that led to LIPSS without surface oxidation. This phenomenon is associated with the material-dependent incubation effect, which leads to a reduction in the material's ablation threshold when the number of pulses per spot increases [36]. The most homogeneous LIPSS obtained at a pulse fluence of 171.2 mJ/cm^2 and an effective number of 209 pulses in ambient environment exhibited a diffracted light intensity of 199.9.
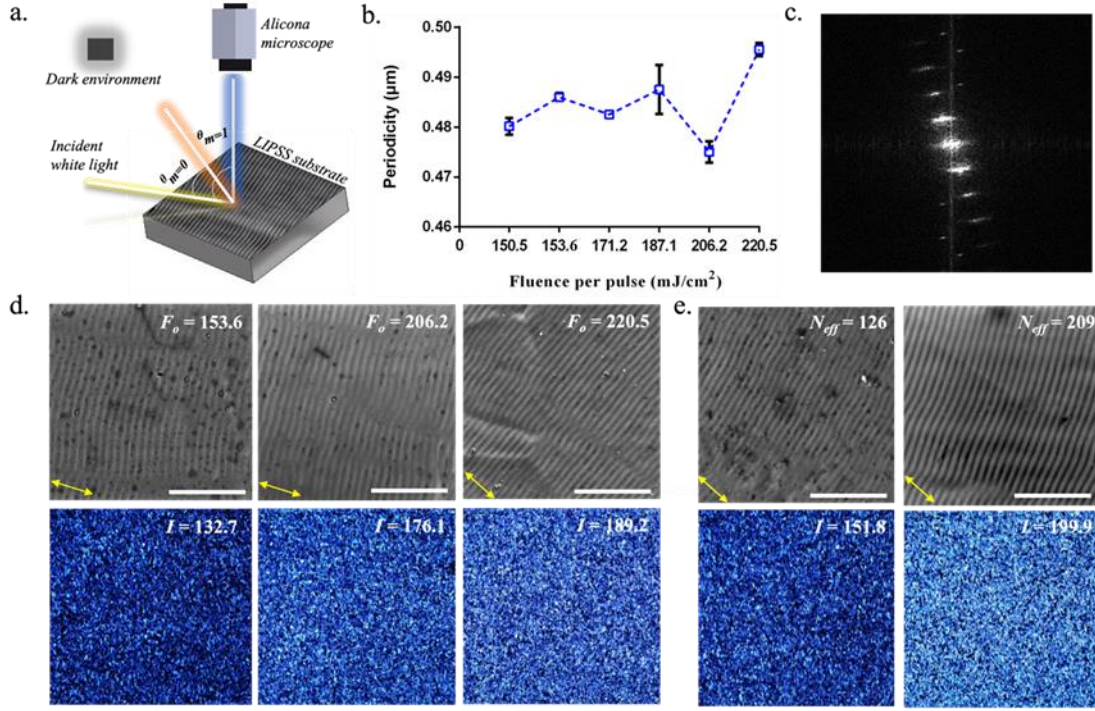
Fig. 3. (a) An illustration of the experimental set-up to obtain first-order diffraction blue light images from LIPSS. (b) The periodicity of LIPSS produced with 209 pulses and pulse fluences varying from 150.5 up to 220.5 mJ/cm^2. (c) 2D FFT image showing the regularity of the LIPSS generated with 209 pulses and pulse fluence of 171.2 mJ/cm^2. The LIPSS formation with (d) the increase of pulse fluence in the range of 153.6 to 220.5 mJ/cm^2 and a constant effective number of pulses set at 126 (scale bar: 5 μm) and (e) the increase of effective number of pulses from 126 to 209 at a constant pulse fluence of 171.2 mJ/cm^2 (scale bar: 5 μm). The corresponding blue light diffraction images are also shown. *Note*: The yellow double-sided arrows represent laser beam polarization vector.

At the same time, irradiation of surfaces with an effective number of 209 pulses and pulse fluences higher than a specific level also led to surface coloration due to the oxidation effects. Fig. 4a shows oxidation colors appearing at different pulse fluences and effective number of pulses. This color generation is caused by the thin film interference phenomena and depends on the thickness of the oxide layer in the laser processed area [37]. For instance, beyond the pulse fluence of 220.5 mJ/cm^2 at an effective number of pulses of 209, the LIPSS started to disappear, and the surface showed a yellow ($F_0 = 320.9$ mJ/cm^2), which is followed by orange ($F_0 = 386.9$ mJ/cm^2) colors. Moreover, a further increase in effective number of pulses to 419 resulted in purple ($F_0 = 386.9$ mJ/cm^2) and blue ($F_0 = 457.0$ mJ/cm^2) colors. Furthermore, the

higher accumulated fluence at the edges of the processed area, where the laser beam had to accelerate/decelerate along its scanning path, led to the appearance of the blue color as shown in Fig. 4b.
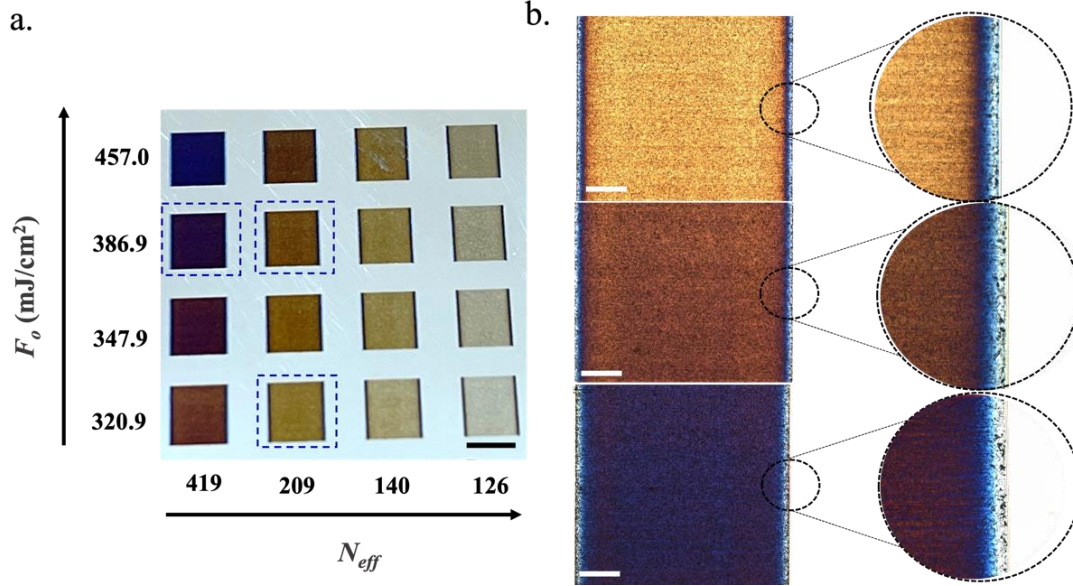

Fig. 4. Oxidation colors on SS substrates: (a) the matrix shows the colors appearing at high pulse fluences and a higher number of pulses (scale bar: 5 mm). (b) The corresponding magnified optical images showing yellow, orange, and purple colors as a result of the increasing accumulated fluence (scale bar: 1 mm). The corresponding inset image shows the blue color at the edge of the squares due to beam deceleration/acceleration and the resulting high accumulated fluence there.

Finally, the threshold value of blue light intensity was set at 160 to determine the quality of LIPSS in this research. Therefore, LIPSS that exhibited $I < 160$ were considered as low-quality ones, whereas those with $I > 160$ were deemed as LIPSS with a satisfactory quality. Fig. 5 shows the map of morphologies obtained within the investigated processing window. The surface morphologies were clustered into four categories, i.e., no LIPSS formation, low- and high-quality LIPSS and excessive oxidation on the surface. Overall, it is worth stating that the accumulated fluence during the LIPSS generation with the green nanosecond laser was identified to be in the range from 13.9 to 46.2 J/cm^2. While the use of laser settings outside this processing window led to either no LIPSS formation or alterations in surface chemistry, i.e., oxidation over the processed area. As can be seen, an effective number of pulses between 105 and 209 led to the generation of high-quality LIPSS on the surface.
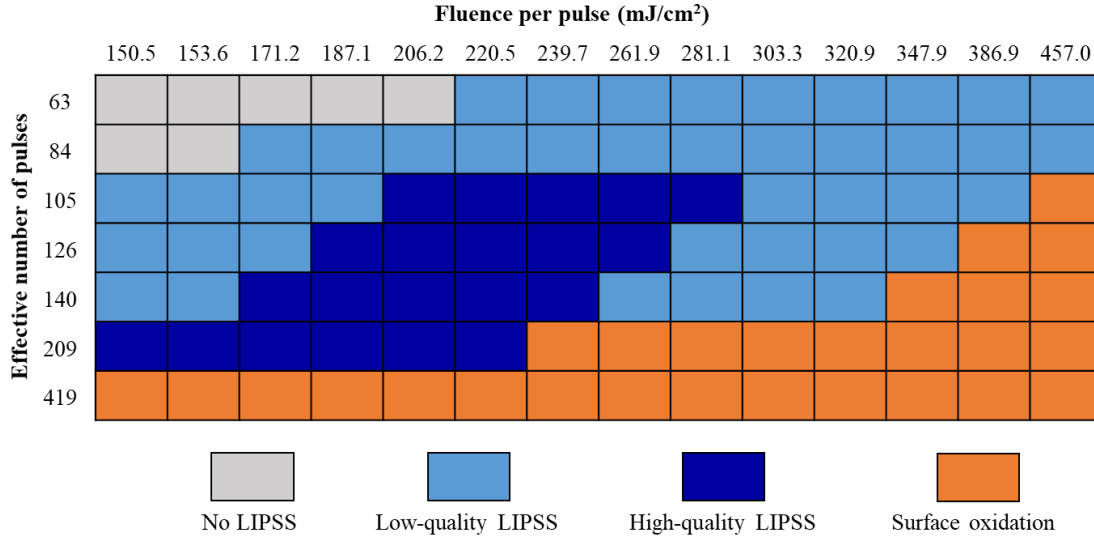
Fig. 5. LIPSS morphologies as a function of the pulse fluence and the effective number of pulses.

3.2 LIPSS quality in argon gas environment

Experiments were also carried out in argon environment with the process parameters used to obtain good quality LIPSS in the ambient one. In particular, the pulse fluences used was in the range from 150.5 mJ/cm^2 to 220.5 mJ/cm^2 with an effective number of pulses were kept the same at 209 during these experiments. Fig. 6a shows SEM images of LIPSS generated in the ambient and argon environments along with their corresponding blue light images. At a pulse fluence of 150.5 mJ/cm^2, the LIPSS topographies were also covered by pits/holes when laser processing was conducted in the ambient environment. In contrast, such defects were not anymore present on LIPSS processed in argon. Consequently, the corresponding blue light images appear to be brighter for the samples produced in argon environment compared to those in the ambient one. When the fluence was increased to 171.2 mJ/cm^2, the LIPSS showed no more defects even in the ambient environment. At the same time, it is worth noting that the LIPSS generated in argon environment were defect-less under the same pulse fluence, too. In both environments, the LIPSS had almost the same periodicities. Although the SEM micrographs show no remarkable differences, the blue light images reveal that LIPSS generated in argon environment are brighter than those in air. When the blue light intensities are plotted at three different pulse fluences as shown in Fig. 6b, it immediately divulges that the quality of LIPSS produced in argon environment is better.
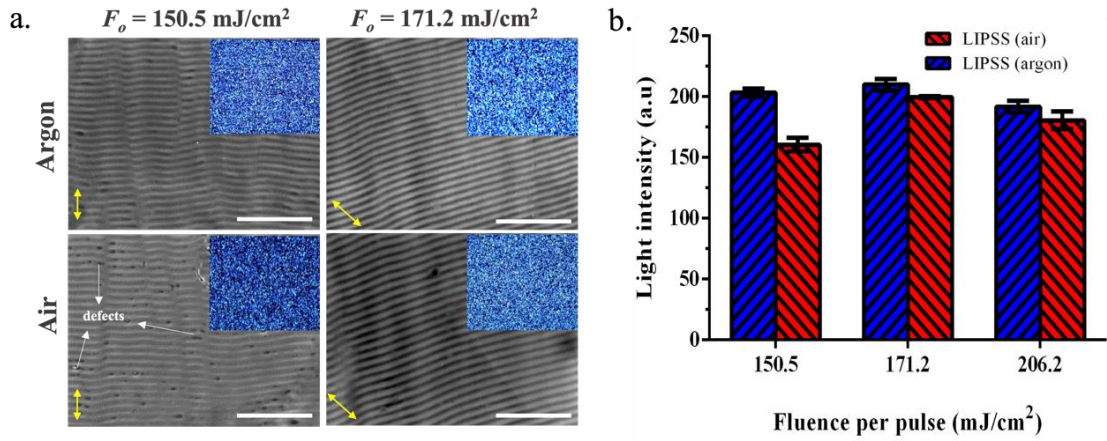
Fig. 6. (a) The SEM images of LIPSS generated under ambient and argon atmospheres with 209 pulses and pulse fluences of 150.5 and 171.2 mJ/cm^2 (scale bar: 5 μm). Their corresponding blue light diffraction images are shown as insets. (b) Comparison of blue light intensities of LIPSS generated with pulse fluences of 150.5, 171.2 and 206.2 mJ/cm^2 and 209 pulses in ambient and argon atmospheres. *Note*: The yellow double-sided arrows show the laser beam polarization vector.
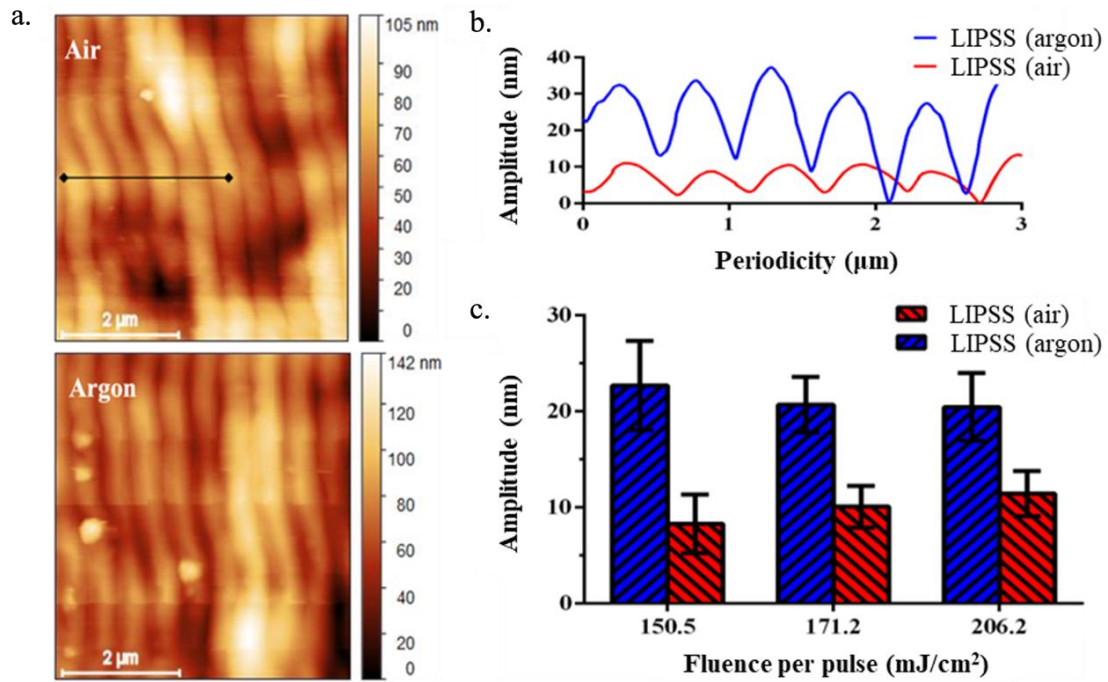

Fig. 7. (a) AFM images of LIPSS and (b) the height profiles of the samples processed in ambient and argon environments at a pulse fluence of 171.2 mJ/cm^2 and an effective number of 209 pulses. (c) The comparison of the LIPSS amplitude at different pulse fluences and a fixed effective number of 209 pulses.

To investigate further the differences in blue light intensities of LIPSS produced in the two environments, AFM measurements were taken to analyze the LIPSS amplitude. Fig. 7a and b present the AFM images of LIPSS together with their extracted height profiles, respectively. It is evident that the LIPSS topographies have higher amplitudes when they were processed in argon than those in air. In particular, the amplitudes vary from 5 to 14 nm and 17 to 27 nm in ambient and argon environments, respectively. This clearly shows that LIPSS generated in argon exhibit heights that are twice higher than those in air. If the mean height of the LIPSS topographies generated in both environments at different pulse fluences are compared, as shown in Fig. 7c, it is obvious that the argon ones exhibit higher aspect ratios. This further underline why the blue light intensity of the samples produced in argon is more pronounced even though the SEM images have shown no discernible differences.

3.3 Surface chemistry analysis

To further understand why the quality of LIPSS differs in argon and ambient environments, XPS analysis was conducted to investigate the alterations in surface chemistry. Fig. 8a-e presents the XPS survey spectrums obtained on the untreated SS substrate and the LIPSS ones processed in both argon and ambient conditions. Here, the LIPSS-I and LIPSS-II are the ones processed with an effective number of pulses of 209 and pulse fluences of 150.5 mJ/cm^2 and 171.2 mJ/cm^2, respectively. A quick look at the spectra shows that oxygen, carbon, chromium, and iron elements dominate on the surface, whereas the influence of other elements, such as nickel and manganese, was not considered as their atomic concentrations were barely quantified. The surface chemical compositions of these LIPSS treated samples are given in Table 1.

Table 1. Elemental composition extracted from the XPS survey spectra of untreated and laser processed SS surfaces.

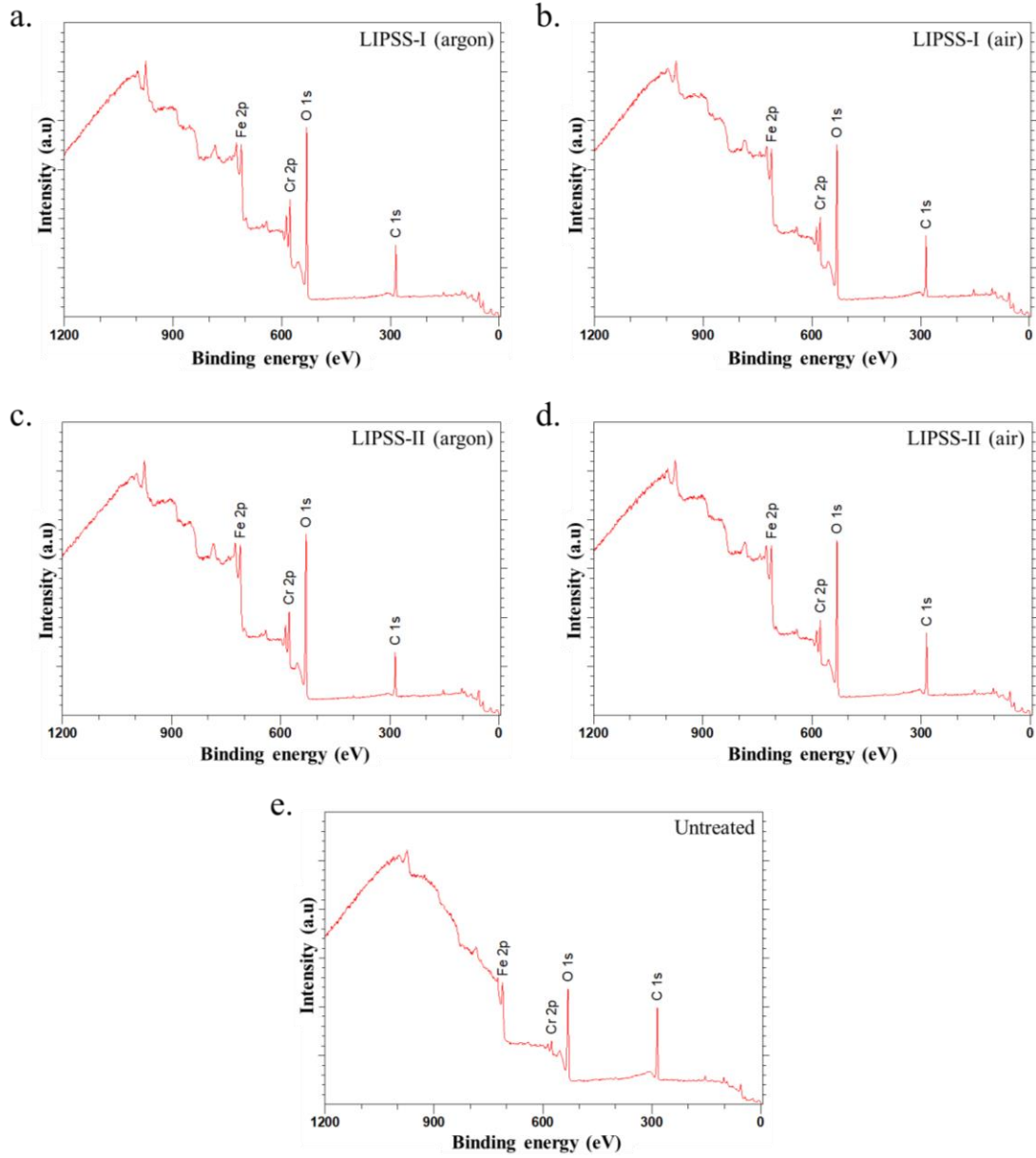| Surface	C (at%)	O (at%)	Fe (at%)	Cr (at%)	O/Fe	O/Cr
Untreated	59.95	35.00	3.50	1.55	10.00	22.58
LIPSS-I (argon)	37.02	46.75	8.64	7.59	5.41	6.16
LIPSS-I (air)	44.33	44.62	6.00	5.05	7.44	8.84
LIPSS-II (argon)	35.05	48.18	10.26	6.51	4.70	7.40
LIPSS-II (air)	45.00	42.79	7.52	4.69	5.69	9.12

Fig. 8. The XPS survey spectra for: (a-d) LIPSS fabricated on SS substrates with 209 pulses and pulse fluences of 150.5 and 171.2 mJ/cm^2 after irradiation in argon and air environments, respectively; (e) untreated SS surface.

The elemental composition of the untreated SS sample is characterized by a higher concentration of carbon compared to oxygen and a significantly low concentration of iron and chromium. The detection of non-zero carbon quantity clearly indicates that this surface was contaminated, and the primary source of such contamination is the adsorption of organic matter from the atmosphere [38]. On the other hand, a remarkable reduction of the carbon content was observed on all laser textured surfaces, which should be attributed to the removal of the pre-existing adventitious carbon during laser irradiation. This cleaning phenomenon was more pronounced on the surfaces processed

in argon and the one treated with a higher pulse fluence resulted in the sharpest decrease of the carbon content. Furthermore, significant variations in the oxygen content were observed among the various analyzed surfaces, too. In particular, the oxygen amount increased together with that of Fe and Cr on the surfaces subjected to laser treatment, especially in those samples processed in argon. However, the ratio of oxygen to iron (O/Fe) and chromium (O/Cr) shows that the LIPSS processed in ambient conditions are oxygen-rich as compared to the ones in argon.
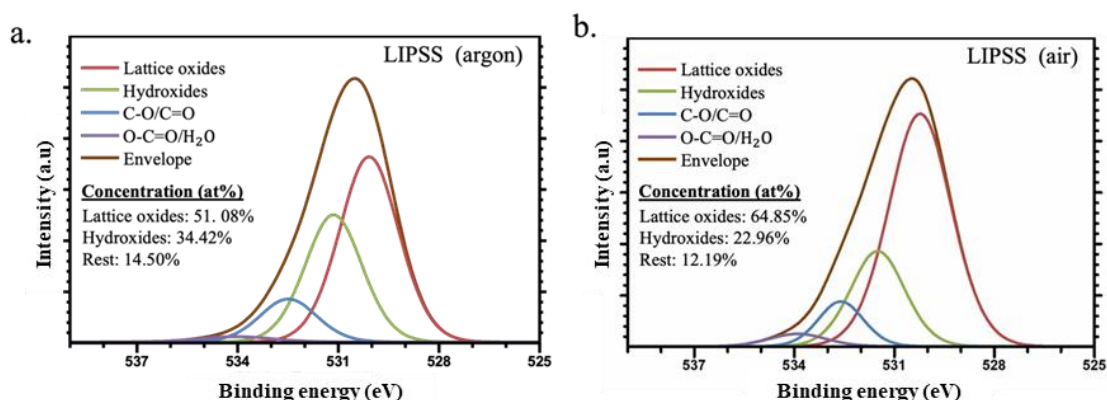

Fig. 9. High-resolution O1s spectra of LIPSS treated under (a) argon and (b) ambient environments.

To evaluate the oxygen contribution, the deconvolution of O1s spectra was analyzed as shown in Fig. 9. It revealed that two contributions related to oxygen in the form of lattice oxides at 530 ± 0.2 eV and hydroxides at 531.5 ± 0.1 eV dominate on the surface while the rest (C-O/C=O at 532.6 ± 0.2 and O-C=O/H_2O at 534 ± 0.2 eV) are minor. As can be seen, most of the oxygen on LIPSS substrates was the result of oxidation reactions, followed by the formation of hydroxides and organic compounds. More specifically, the concentration of lattice oxides was found to be greater on the laser-treated surfaces, while they dominated in those processed in air. It can be inferred that the LIPSS generation led to the exposure of more Fe and Cr from the bulk to the ambient air, which instantly reacted and formed a mixed oxide layer at the surface. On the other hand, the hydroxides had more contribution to the LIPSS processed in argon.

To determine the reason for more hydroxide formation on the LIPSS generated in argon, the high-resolution spectra of metallic elements were also analyzed. The Cr2p (3/2, 1/2) XPS spectra as extracted from the laser-treated surfaces are presented in Fig. 10a, where the resultant positions of the major components are specified. In all the cases, the existence of Cr (III) oxide, Cr_2O_3, was observed on the surfaces at a binding

energy of 576.6 eV. However, a second maxima was presented on all the laser-treated surfaces at around 577.1 eV and it is more pronounced on the LIPSS textured in argon, which most likely is ascribed to the hydroxides $Cr(OH)_3$. On the other hand, by analyzing the Fe2p spectrum as shown in Fig. 10b, it can be inferred that the Fe (III) oxide state, Fe_2O_3, dominates on all the surfaces at a peak position of 711 eV. This observation can also be verified by the weak satellite peak situated at around 719 eV, which is characteristic of Fe (III) oxide. At the same time, the contribution of Fe (II) oxide components, FeO, at a binding energy of approximately 709 eV was more pronounced on the surfaces subjected to laser treatment. Among these surfaces, no distinguishable signal of Cr or Fe in the metallic state was observed over the background noise on the substrates processed in air, which can confirm the formation of a uniform oxide layer on their surfaces. On the other hand, it should be highlighted that the samples processed in argon gas had some contribution of pure metallic components at 707 eV and thus the thickness of the oxide layer on these surfaces was less than 10 nm (the photoelectron's penetration depth in XPS measurements) [39]. This observation underlines that the thickness of the oxide layer has contributed to less depth of ripples in LIPSS processed in the air as evident from the AFM measurements.
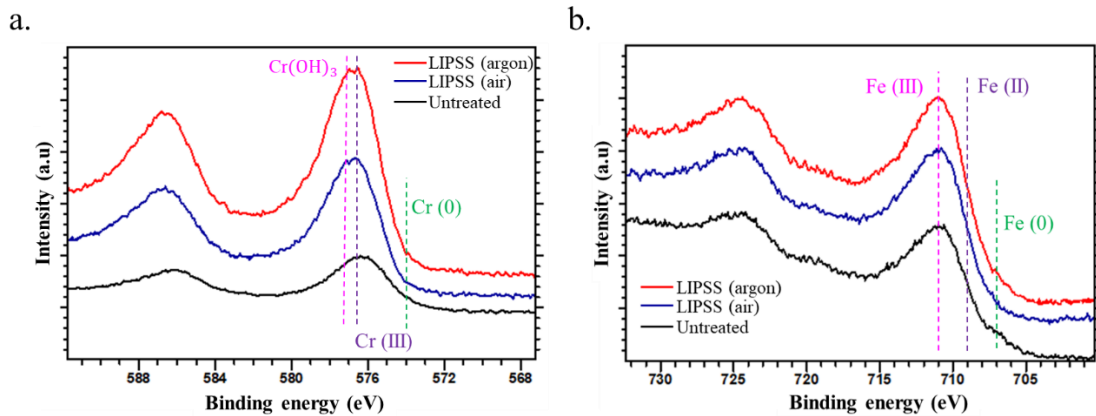

Fig. 10. High-resolution XPS spectra of (a) Cr2p and (b) Fe2p of untreated surface and LIPSS generated in argon and ambient environments.

Based on the observations from first-order diffraction response (blue light intensity), surface topography (SEM and AFM) and chemistry (XPS) responses, Fig. 11 illustrates evidently the processing environment influence on surface topography and chemistry at low and high accumulated fluences. Apparently, at low accumulated fluences (< 50.1 J/cm^2), the interaction of the green nanosecond laser beam with the SS surface results in the formation of LIPSS in ambient environment. However, the formation of a thin

layer of oxide during the processing suppresses the amplitude of the LIPSS. A change of processing environment to argon decreases the thickness of the oxide layer, which is evident from the decrease in oxygen content (O/Fe ratio) as shown in Table 1. The thickness of the oxide layer (t) can be estimated to be less than 20 nm, as evident from AFM profiles of LIPSS produced in ambient and argon environments (see Fig. 7b). On the other hand, high accumulated fluences ($\geq$ 50.1 J/cm^2) generate roughness on the substrate along with a thick oxide layer. For instance, a recent investigation onto green nanosecond laser coloring of stainless steel surfaces in an ambient environment showed that the oxide film thickness varies from 200 to 600 nm, which led to different colors [40]. At the same time, the surface roughness of these thick oxide covered areas ranged from 0.5 to 1.2 μm.
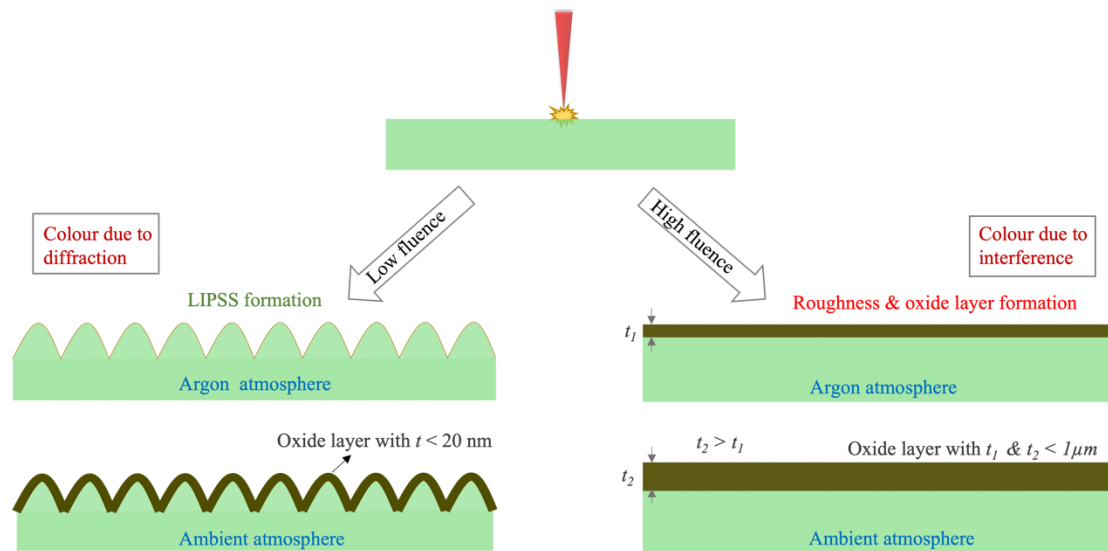

Fig. 11. An illustration showing the influence of processing environment on oxide layer formation at low and high accumulated fluences with a green nanosecond laser.

3.4 Contact angle analysis

To investigate the combined influence of surface topography and chemistry on macroscopic properties, the contact angle measurements were conducted on the LIPSS surfaces produced in air and argon environments. Contact angle variations over a period of two weeks on the surfaces are shown in Fig. 12. On the untreated SS surface, the contact angle was measured to be 71.2º ± 1.2º. It is apparent that the contact angle decreased immediately after the LIPSS treatment in both air and argon environments. The magnitude of this decrease is more on the surfaces that were processed in argon when compared to those treated in air. However, the contact angle gradually increased

18

on both LIPSS topographies after day 3 and reached a maximum of $90.8^{o} \pm 2.8^{o}$ in argon exhibiting hydrophobicity.
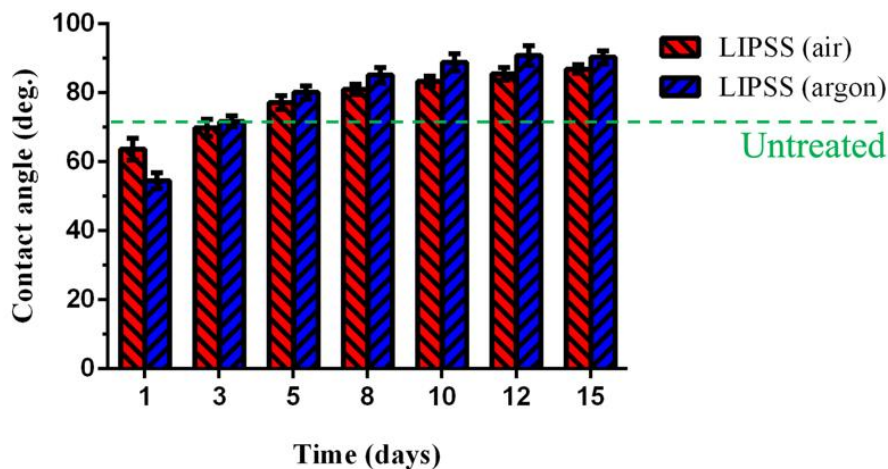

Fig. 12. Contact angle evolution as a function of time in number of days on untreated and LIPSS treated substrates in the air and argon environments.

One of the key indicators of surface chemistry to determine the wetting state is the oxygen-to-carbon ratio (O/C) on the surfaces, which influences the contact angle of the laser-treated surfaces [41]. The lack of oxygen species on the surfaces processed in argon exhibited a lower contact angle immediately after laser processing. However, over a period of time, the CO_2 decomposes from the atmosphere and hence the O/C ratio increases on the surfaces. The decomposition of CO_2 leads to a transfer of O^{2-} ions to oxygen-deficient magnetite $Fe_3O_{4-\delta}$ $(0 < \delta < 1)$ and results in the formation of Fe_3O_4 [42]. On the surfaces processed in argon, the decomposition of CO_2 favors the formation of Fe_3O_4 and the surface becomes rich in oxygen-to-carbon ratio. For instance, the O/C on samples processed in argon is 1.2 - 1.3 whereas on the ones treated in the air is 0.9 - 1.0. At the same time, the LIPSS are deeper in the samples processed in argon than those in air. Therefore, the combined effects of topography and surface chemistry have led to an increase in the contact angle on LIPSS generated in an argon environment. However, it should also be noted that the magnitude of the difference is not significant between the ones processed in argon and air as the LIPSS exhibit a low roughness factor (a ratio of actual surface area to the projected one).

4. Conclusions

Laser texturing/structuring of surfaces with LIPSS topographies has been extensively deployed as a means for tailoring their functional characteristics. However, the

generation of high-quality homogeneous LIPSS cost-effectively on relatively large surfaces is an important step toward the broader use of this technology for functionalizing surfaces at an industrial scale. In this research, a green nanosecond laser was investigated for producing LIPSS on AISI 316 stainless steel under air and argon environments. The quality of LIPSS generated in both environmental conditions was evaluated through the SEM, AFM and XPS analysis and correlated with their blue light diffraction response. In an argon environment, the intensity of the diffracted light increased, and this was indicative of the improved quality and homogeneity of LIPSS generated on the surfaces. The relatively low-quality LIPSS produced in the air can be attributed to the formation of oxides as a side effect compared to the laser processing in argon. Since the intensity of the first-order diffracted light depends only on the LIPSS periodicity and depth and not on the surface chemistry, the topographical changes (e.g., periodicity/depth) of the LIPSS could be qualitatively captured by first-order diffracted light (blue light intensity). Therefore, the blue light intensity can act as a global/macroscopic parameter to judge about the quality of the LIPSS, instead of time consuming local measurements, such as SEM/AFM. A higher blue light intensity is indicative of better quality LIPSS, which means that LIPSS are deeper and devoid of pits.

Moreover, the high amplitude LIPSS produced in argon environment could be used for texturing replication masters that can find applications in soft/compression and injection molding. For instance, such masters with high aspect ratio LIPSS treatments could be utilized for producing high quality textured replicas through micro injection molding [43]. At the same time, considering these capabilities for producing sub-wavelength nanostructures, i.e., LIPSS with the green nanosecond laser, such LIPSS treatments can be used to enhance the antireflection properties of surfaces on various materials. Thus, the proposed nanosecond laser treatment in this research could be a potentially cost-effective solution for fabricating functional nanostructured surfaces that can find applications in energy storage, optoelectronics and sensors. For instance, one such application could be to design broad-band ultralow optical reflective surfaces. Future in-depth research will be conducted to explore the optical properties of the nanostructured surfaces. At the same time, the fabrication of multi-scale structures (LIPSS on top of microscale structures) could be an interesting step towards designing

cost-effective superhydrophobic metallic surfaces for anti-bacterial and anti-icing applications.

References

[1]   S. Zhang, Y. Zhou, H. Zhang, Z. Xiong, and S. To, "Advances in ultra-precision machining of micro-structured functional surfaces and their typical applications," *International Journal of Machine Tools and Manufacture,* vol. 142, pp. 16-41, 2019.

[2]   Y.-Y. Quan, Z. Chen, Y. Lai, Z.-S. Huang, and H. Li, "Recent advances in fabricating durable superhydrophobic surfaces: a review in the aspects of structures and materials," *Materials Chemistry Frontiers,* vol. 5, no. 4, pp. 1655-1682, 2021.

[3]   M. Liu, M.-T. Li, S. Xu, H. Yang, and H.-B. Sun, "Bioinspired Superhydrophobic Surfaces via Laser-Structuring," *Frontiers in Chemistry,* vol. 8, no. 835, 2020.

[4]   A. Samanta, Q. Wang, S. K. Shaw, and H. Ding, "Roles of chemistry modification for laser textured metal alloys to achieve extreme surface wetting behaviors," *Materials & Design,* vol. 192, p. 108744, 2020.

[5]   C. Florian, S. V. Kirner, J. Krüger, and J. Bonse, "Surface functionalization by laser-induced periodic surface structures," *Journal of Laser Applications,* vol. 32, no. 2, p. 022063, 2020.

[6]   Y.-F. Gao *et al.*, "Picosecond laser-induced periodic surface structures (LIPSS) on crystalline silicon," *Surfaces and Interfaces,* vol. 19, p. 100538, 2020.

[7]   M. J. Kang *et al.*, "Periodic surface texturing of amorphous-Si thin film irradiated by UV nanosecond laser," *Opt. Mater. Express,* vol. 9, no. 11, pp. 4247-4255, 2019.

[8]   R. Y. Siddiquie, A. Gaddam, A. Agrawal, S. S. Dimov, and S. S. Joshi, "Anti-Biofouling Properties of Femtosecond Laser-Induced Submicron Topographies on Elastomeric Surfaces," *Langmuir,* vol. 36, no. 19, pp. 5349-5358, 2020.

[9]   X. Luo *et al.*, "Biocompatible nano-ripples structured surfaces induced by femtosecond laser to rebel bacterial colonization and biofilm formation," *Optics & Laser Technology,* vol. 124, p. 105973, 2020.

[10]   A. Gaddam, H. Sharma, T. Karkantonis, and S. Dimov, "Anti-icing properties of femtosecond laser-induced nano and multiscale topographies," *Applied Surface Science,* vol. 552, p. 149443, 2021.

[11]   S. Sarbada, Z. Huang, Y. C. Shin, and X. Ruan, "Low-reflectance laser-induced surface nanostructures created with a picosecond laser," *Applied Physics A,* vol. 122, no. 4, p. 453, 2016.

[12]   A. Gaddam, H. Sharma, R. Ahuja, S. Dimov, S. Joshi, and A. Agrawal, "Hydrodynamic drag reduction of shear-thinning liquids in superhydrophobic textured microchannels," *Microfluidics and Nanofluidics,* vol. 25, no. 9, p. 73, 2021.

[13]   T. Karkantonis, A. Gaddam, T. L. See, S. S. Joshi, and S. Dimov, "Femtosecond laser-induced sub-micron and multi-scale topographies for durable lubricant impregnated surfaces for food packaging applications," *Surface and Coatings Technology,* vol. 399, p. 126166, 2020.

[14]   J. J. J. Nivas *et al.*, "Secondary electron yield reduction by femtosecond pulse laser-induced periodic surface structuring," *Surfaces and Interfaces,* vol. 25, p. 101179, 2021.

[15]   M. Martínez-Calderon *et al.*, "Surface micro- and nano-texturing of stainless steel by femtosecond laser for the control of cell migration," *Scientific Reports,* vol. 6, no. 1, p. 36296, 2016.

[16]   A. Batal, R. Sammons, and S. Dimov, "Response of Saos-2 osteoblast-like cells to laser surface texturing, sandblasting and hydroxyapatite coating on CoCrMo alloy surfaces," *Materials Science and Engineering: C,* vol. 98, pp. 1005-1013, 2019.

[17]   A. Velic, J. Hasan, Z. Li, and P. K. D. V. Yarlagadda, "Mechanics of Bacterial Interaction and Death on Nanopatterned Surfaces," *Biophysical Journal,* vol. 120, no. 2, pp. 217-231, 2021.

[18]   L. Bao, N. V. Priezjev, and H. Hu, "The local slip length and flow fields over nanostructured superhydrophobic surfaces," *International Journal of Multiphase Flow,* vol. 126, p. 103258, 2020.

[19]   S. Ahmad, H. Sharma, A. Agrawal, and S. S. Joshi, "Light Harvesting Using Biomimetic Micro-textured Transparent Films for Photovoltaic Applications," *Transactions of the Indian National Academy of Engineering,* vol. 6, no. 3, pp. 775-785, 2021.

[20]   M. Hiratsuka, M. Emoto, A. Konno, and S. Ito, "Molecular Dynamics Simulation of the Influence of Nanoscale Structure on Water Wetting and Condensation," *Micromachines,* vol. 10, no. 9, p. 587, 2019.

[21]   A. Batal, A. Michalek, P. Penchev, A. Kupisiewicz, and S. Dimov, "Laser processing of freeform surfaces: A new approach based on an efficient workpiece partitioning strategy," *International Journal of Machine Tools and Manufacture,* vol. 156, p. 103593, 2020.

[22]   A. Michalek *et al.*, "Modelling ultrafast laser structuring/texturing of freeform surfaces," *Applied Surface Science Advances,* vol. 2, p. 100036, 2020.

[23]   O. Hofmann, J. Stollenwerk, and P. Loosen, "Design of multi-beam optics for high throughput parallel processing," *Journal of Laser Applications,* vol. 32, no. 1, p. 012005, 2020.

[24]   G. Bonamis *et al.*, "High efficiency femtosecond laser ablation with gigahertz level bursts," *Journal of Laser Applications,* vol. 31, no. 2, p. 022205, 2019.

[25]   D. Bhaduri *et al.*, "Laser polishing of 3D printed mesoscale components," *Applied Surface Science,* vol. 405, pp. 29-46, 2017.

[26]   C. P. Ma, Y. C. Guan, and W. Zhou, "Laser polishing of additive manufactured Ti alloys," *Optics and Lasers in Engineering,* vol. 93, pp. 171-177, 2017.

[27]   Z. Yang, Y. Tian, Y. Zhao, and C. Yang, "Study on the Fabrication of Super-Hydrophobic Surface on Inconel Alloy via Nanosecond Laser Ablation," *Materials,* vol. 12, no. 2, p. 278, 2019.

[28]   J. S. Hwang, J.-E. Park, G. W. Kim, H. Lee, and M. Yang, "Fabrication of printable nanograting using solution-based laser-induced periodic surface structure process," *Applied Surface Science,* vol. 547, p. 149178, 2021.

[29]   P. Nürnberger *et al.*, "Influence of substrate microcrystallinity on the orientation of laser-induced periodic surface structures," *Journal of Applied Physics,* vol. 118, no. 13, p. 134306, 2015.

[30]   J. G. A. B. Simões, R. Riva, and W. Miyakawa, "High-speed Laser-Induced Periodic Surface Structures (LIPSS) generation on stainless steel surface using a nanosecond pulsed laser," *Surface and Coatings Technology,* vol. 344, pp. 423-432, 2018.

[31]   P. Nürnberger *et al.*, "Orthogonally superimposed laser-induced periodic surface structures (LIPSS) upon nanosecond laser pulse irradiation of SiO2/Si layered systems," *Applied Surface Science,* vol. 425, pp. 682-688, 2017.

[32]   S. Y. Son *et al.*, "In-depth optical characterization of poly(3-hexylthiophene) after formation of nanosecond laser-induced periodic surface structures," *Nanoscale,* 10.1039/C8NR10075F vol. 11, no. 16, pp. 7567-7571, 2019.

[33]   S. Durbach and N. Hampp, "Generation of 2D-arrays of anisotropically shaped nanoparticles by nanosecond laser-induced periodic surface patterning," *Applied Surface Science,* vol. 556, p. 149803, 2021.

[34]   H. M. Reinhardt, P. Maier, H.-C. Kim, D. Rhinow, and N. Hampp, "Nanostructured Transparent Conductive Electrodes for Applications in Harsh Environments Fabricated via Nanosecond Laser-Induced Periodic Surface Structures (LIPSS) in Indium–Tin Oxide Films on Glass," *Advanced Materials Interfaces,* vol. 6, no. 16, p. 1900401, 2019.

[35]   J. Eichstädt, G. R. B. E. Römer, and A. J. Huis in 't Veld, "Determination of irradiation parameters for laser-induced periodic surface structures," *Applied Surface Science,* vol. 264, pp. 79-87, 2013.

[36]   Z. Sun, M. Lenzner, and W. Rudolph, "Generic incubation law for laser damage and ablation thresholds," *Journal of Applied Physics,* vol. 117, no. 7, p. 073102, 2015.

[37]   H. Liu, W. Lin, and M. Hong, "Surface coloring by laser irradiation of solid substrates," APL Photonics, vol. 4, no. 5, p. 051101, 2019.

[38]   S. Tardio, M.-L. Abel, R. H. Carr, J. E. Castle, and J. F. Watts, "Comparative study of the native oxide on 316L stainless steel by XPS and ToF-SIMS," *Journal of Vacuum Science & Technology A,* vol. 33, no. 5, p. 05E122, 2015.

[39]   G. Li *et al.*, "Evolution of aluminum surface irradiated by femtosecond laser pulses with different pulse overlaps," *Applied Surface Science,* vol. 276, pp. 203-209, 2013.

[40]   X. Ma et al., "Effect of nanosecond pulsed laser parameters on the color making of 304 stainless steel," Optics & Laser Technology, vol. 126, p. 106104, 2020.

[41] A. Žemaitis *et al.*, "Controlling the wettability of stainless steel from highly-hydrophilic to super-hydrophobic by femtosecond laser-induced ripples and nanospikes," *RSC Advances,* vol. 10, no. 62, pp. 37956-37961, 2020.

[42] A.-M. Kietzig, S. G. Hatzikiriakos, and P. Englezos, "Patterned Superhydrophobic Metallic Surfaces," *Langmuir,* vol. 25, no. 8, pp. 4821-4827, 2009.

[43] F. Baruffi *et al.*, "Correlating nano-scale surface replication accuracy and cavity temperature in micro-injection moulding using in-line process control and high-speed thermal imaging," *Journal of Manufacturing Processes,* vol. 47, pp. 367-381, 2019.